Upper mantle seismic wave attenuation: Effects of realistic partial melt distribution

William C. Hammond and Eugene D. Humphreys
Department of Geological Sciences, University of Oregon, Eugene

Abstract

Frequency dependence of seismic velocity and attenuation resulting from viscoelastic relaxation of partially molten mantle is estimated. We consider the contribution of the melt squirt mechanism, through which pressure differences between disk-shaped inclusions are equalized by melt passing through connecting tubes. The pressure differences arise as a result of shear strain compressing disk-shaped pores differently on the basis of disk orientation with respect to the applied shear. The frequencies over which the transition from the unrelaxed to the relaxed states occurs are determined by representing the melt as a network of tubes connecting oblate ellipsoidal pores. The pressure equalization process is modeled by a system of first-order linear differential equations, whose eigenvalues are the characteristic frequencies for melt squirt relaxation. It is shown that in this framework the set of frequencies is invariant to the absolute scale of the system but is sensitive to melt bulk modulus and viscosity, as well as distribution of melt inside pores and conduits. Use of realistic solid and melt physical properties and pore and conduit geometries demonstrates that it is the relaxed modulus that is most likely excited in the seismic band and that melt mobility has little effect on seismic attenuation. Some conceivable melt distributions, however, would result in detectable attenuation in the seismic band. In all cases investigated, attenuation increases with frequency, indicating that melt squirt is not responsible for global upper mantle Q observations.

1. Introduction

Measurements of body waves, surface waves, normal modes, and the behavior of laboratory samples have provided constraints on the magnitude, distribution and frequency dependence of attenuation in the Earth. Studies of anelasticity in the mantle have shown a roughly constant Q or weak dependence of Q on frequency [*Jackson and Anderson*, 1970; *Kanamori and Anderson*, 1977; *Karato and Spetzler*, 1990]:

$$Q \sim \omega^{\alpha}, \qquad (1)$$

where $\alpha \sim 0.1$ to 0.3 for frequencies from 10^{-8} to 1 Hz. Above 1 Hz, there is some evidence that Q has an approximately linear dependence on ω [*Solomon and Toksöz*, 1970; *Kanamori and Anderson*, 1977; *Anderson and Given*, 1982]. Low values for Q [*Anderson and Hart*, 1978] and low velocities at depths between 25 and 200 km in the ocean basins [*Cara*, 1979; *Nishimura and Forsyth*, 1989; *Webb and Forsyth*, 1998] have been seen as evidence that melt may be present at these depths. Positive identification of melt has proven elusive, however, owing to difficulties in separating anharmonic (frequency independent and nonattenuating) and anelastic (attenuating and frequency-dependent) components of velocity reduction, and in separating the effects of solid-state attenuation from those of partial melt [e.g., *Sobolev et al.*, 1996].

Stress relaxation of mantle rock with a small percentage of partial melt is characterized by the presence of numerous sets of potential solid-state and liquid mechanisms, each with its own range of relaxation times. Above the solidus temperature, possible contributions to attenuation arise from viscous shear relaxation of the melt, melt squirt, melt-enhanced grain boundary sliding, and solid-state dislocation and diffusion within crystals. In this paper we do not consider the effects of solid-state creep in the seismic frequency band as this has been discussed elsewhere [e.g., *Karato and Spetzler*, 1990]. We presume that under realistic conditions (i.e., low attenuation) the solid-state and the melt-related contributions to attenuation are approximately additive. Given realistic melt viscosity and inclusion aspect ratios, viscous shear relaxation of the fluid occurs far too quickly to provide attenuation in the seismic frequency band [*O'Connell and Budianski*, 1977; *Schmeling*, 1985].

Although it has been found that grain boundary deformation processes are important at tectonic strain rates [*Hirth and Kohlstedt*, 1995a, b], no data relevant to seismic frequencies exist on the influence of melt-enhanced grain boundary sliding accommodated by dislocation and diffusion creep. Thus, here we focus on the effect of the melt squirt mechanism to reduction of the shear modulus and absorption of energy.

Past efforts to describe the effect of melt on the frequency dependence of attenuation have included those of *O'Connell and Budianski* [1977], *Mavko* [1980], and *Schmeling* [1985]. These studies have relied on models that identify relaxation times on the basis of simple models for the connectivity of the melt. Connectivity of melt inclusions has been approximated as (1) intersecting cracks, (2) fluid inclusions connected by simply shaped conduits, or (3) fluid inclusions communicating through a permeable medium. One feature shared by these studies is that relaxation times were found to be too short (10^{-6} to 10^{-2} s) to provide attenuation in the seismic frequency band (10^{-2} to 10^{1} Hz). One exception to this is the result of *Mavko* [1980] that given melt partitioned into 10% cuspate, triple junction-like tubes, and 90% in the connected pores, the characteristic frequencies begin to enter the high-frequency end of the seismic band. Here we adopt a similar model in that volumetrically, the melt is contained mostly in low aspect ratio disc-like pores, connected by a smaller percentage of melt in the form of narrow cuspate tubes. This view of the melt phase is motivated by experimental results where partial melt textures have been analyzed in detail [*Waff and Bulau*, 1979; *Kohlstedt*, 1992; *Faul et al.*, 1994]. An important effect of the melt phase being partitioned in this manner is that when shear stresses are applied externally, large amounts of melt are forced through relatively long narrow conduits, thereby increasing the importance of longer relaxation time constants in the system.

"Melt squirt," a term coined by *Mavko and Nur* [1975], refers to relaxation occurring when pressure differences between neighboring inclusions drive fluid flow. The pressure gradients are induced when external shear is imposed, variably pressurizing inclusions of different orientations. As discussed below, hydrostatic compression is not likely to create measurable attenuation in the seismic band, so bulk effects are not considered here in detail. The timescale of fluid pressure equalization controls the frequencies over which melt squirt is important. This equalization time is dependent on the geometry of inclusions and connecting conduits, viscosity of the melt, and compressibility of the melt and surrounding rock.

In the following, we model the frequency dependence of seismic velocity and attenuation by calculating the spectrum of characteristic relaxation frequencies resulting from melt squirt. A representation of the melt as a network of realistically shaped conduits joining ellipsoidal pores is used. With this type of representation it is possible to evaluate the effect of any discrete form of melt connectivity, or set of physical parameters. We select three end-member possibilities for melt distribution and determine their relaxation spectra and their effect on seismic velocity and attenuation. Each case is evaluated for its potential to produce significant attenuation in the seismic band.

2. Modeling Material Properties: Basic Relations

In response to a step function in applied shear strain a sequence of stress states in the partially molten rock can be recognized. These discrete stages of melt relaxation are illustrated in Figure 1. Initially, when external shear is applied, the instantaneous response, i.e., the "glued" case [*O'Connell and Budianski*, 1977] is the elastic state occurring before any shear stresses inside the melt have dissipated (Figure 1d). Viscous relaxation inside melt inclusions is the transition from the glued state to the "unrelaxed" state (Figure 1e). Since the viscosity of melt is near 100 Pa s, and the shear modulus is of the order of gigapascals, the times associated with relaxation of shear stresses inside melt pockets are very short, and the associated frequencies lie far above the seismic band. Thus we do not consider this mechanism here. As the melt shear stresses relax, differences in pore pressure arise in the separate inclusions as a result of the variety of inclusion shapes and orientations (Figure 1e). This state, in which fluid flow between inclusions has not yet equalized pressure, is known as the unrelaxed state, or alternatively as the "isolated" case. In response to these pressure differences, fluid flow passes through the conduits connecting the pores. The stress state after all interinclusion fluid flow has occurred is the "relaxed" or "isobaric" state (Figure 1f). The set of timescales over which the system relaxes defines the spectrum of frequencies important for melt squirt attenuation and velocity reduction.

The frequency-dependent seismic wave velocity reduction and attenuation can be determined from the time domain response by calculating the frequency-dependent complex elastic modulus of the two-phase material. The behavior of a (massless) viscoelastic substance can be obtained from the transient stress response excited by a step function in strain. To this end, the stress creep function $\phi(t)$ that describes the exponential decay of stress (Figure 1b) is introduced and is defined by

$$\sigma(t) = M_u \varepsilon_0 [1 + \phi(t)], \qquad (2)$$

where σ is the stress in the material, ε_0 is the applied shear strain, and $\phi(0) = 0$. M_u is the unrelaxed modulus of the material, defined by (2) when $t = 0$. The function $\phi(t)$ is a unitless function that contains all the information about the character of decay of stress in the material. M_r is the relaxed modulus that is characteristic of the final state of relaxation so $\phi(\infty) = M_r/M_u - 1$. The Fourier transform of the stress creep response time derivative is related to the complex elastic modulus by

$$M(\omega) = M_u[1 + \int_0^\infty e^{i\omega t} \dot{\phi}(t) dt], \qquad (3)$$

adapted from *Aki and Richards* [1980, p. 178] with applied strain rather than applied stress. The superscript dot is the time derivative, introduced because the input is a step function, not a delta function strain. A complex component of the elastic modulus represents the presence of attenuation and phase delay for each harmonic driving function. The absorption factor Q^{-1} is defined as

$$Q^{-1} = \frac{\text{Im(M)}}{\text{Re(M)}}. \qquad (4)$$

In practice, as a matter of computational convenience, we use an approximation that allows us to calculate $M(\omega)$ and $Q^{-1}(\omega)$ directly, without finding $\phi(t)$ explicitly, provided we can obtain the relaxed M_r and unrelaxed M_u moduli and the set of characteristic frequencies ω_k that control melt squirt relaxation. This is discussed more completely in section 3.

3. Network Representation

We determine the frequency dependent attenuation resulting from the melt squirt mechanism by modeling the melt phase as randomly oriented biaxial oblate ellipsoidal pores connected by tubes. The analysis of *Faul et al.* [1994] has shown that for melt fractions between 0.8 and 3.3 vol %, most of the melt is contained in low aspect ratio disk-shaped pores. If these pores are randomly distributed, they will be differentially pressurized according to their

(a) $\varepsilon(t)$ t=0

(b) $\sigma(t)$ σ_u σ_r t=0

time→

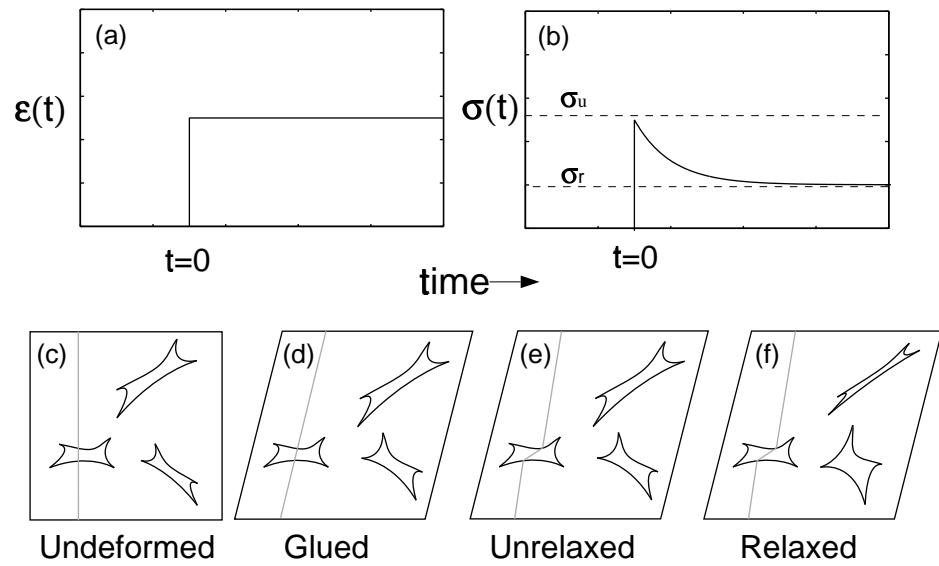(c) Undeformed   (d) Glued   (e) Unrelaxed   (f) Relaxed

Figure 1: Hammond and Humphreys [2000b]

orientation with respect to the sense of macroscopic shear. Low aspect ratio three-grain boundary inclusions ("tubules") also are present and are likely to control permeability when the melt fraction is below the percolation threshold of the larger disk-shaped inclusions, probably near 3% melt fraction [*Faul*, 1997]. Thus we model disk-like inclusions as ellipsoidal pores, which are connected by the conduits that represent the three-grain boundary tubules.

The coordination of connection between the pores has a role in determining the spectrum of relaxation times, so it is important that the selected network configuration is representative of mantle partial melts. We have chosen Kelvin's tetrakaidecahedral (truncated octohedron), which when close packed is a space-filling polyhedron whose grain boundaries simulate the coordination of partial melt contained in the interstitial spaces of olivine crystals (Figure 2). This shape was first used to represent mantle melts by *Frank* [1968] and was later used by *Mavko* [1980] and *Waff* [1980]. Three grains of this shape contact to form a linear intersection, representing a tube where melt resides. Four triplejunction tubules come together at four-grain contact points, approximating the coordination of mantle melts.

The relationship between the flux of melt through the conduits and the physical parameters of the system is given by

$$\frac{d\mathbf{\Phi}}{dt} = \mathbf{G}\mathbf{\Phi}, \tag{5}$$

$$\mathbf{G} = -\frac{K_m}{\eta \kappa S}\mathbf{R}^{-1}\mathbf{\Gamma}\mathbf{V}^{-1}\mathbf{\Gamma}^{\mathbf{T}} \tag{6}$$

(see Appendix A). In this relation, $\mathbf{\Phi} = \mathbf{\Phi(t)}$ is a vector of the melt fluxes through the conduits, K_m is melt bulk modulus, η is fluid viscosity, and κ is a parameter that adjusts tube impedance based on its deviation from a circular cross section. The pore volumes are stored in diagonal matrix $\mathbf{V}$, the connectivity network is stored in matrix $\mathbf{\Gamma}$, and the generalized conduit impedances to fluid flow are stored in diagonal matrix $\mathbf{R}$. The parameter S is the fractional change in hydrostatic strain of the melt, associated with transition from the unrelaxed to the relaxed state.

This linear system of first-order differential equations has general solutions of the form

$$\mathbf{\Phi}_k(t) = e^{-\omega_k t}\mathbf{u}_k, \tag{7}$$

where ω_k are the eigenvalues of the matrix $\mathbf{G}$ and $\mathbf{u}_k$ are the corresponding eigenvectors. Particular solu-

tions require knowledge of the initial conditions of the system. The complete solution is

$$\mathbf{\Phi}(t) = \sum_{k=1}^{n} c_k e^{-\omega_k t}\mathbf{u}_k, \tag{8}$$

where

$$\mathbf{c} = \mathbf{U}^{-1}\mathbf{\Phi}(0) \tag{9}$$

and where $\mathbf{U}$ is a matrix whose columns are the $\mathbf{u}_k$. In the unrelaxed state the initial fluxes are

$$\mathbf{\Phi}(0) = \frac{1}{\eta\kappa}\mathbf{R}^{-1}\mathbf{\Gamma}\mathbf{P}(0), \tag{10}$$

where $\mathbf{P}(0)$ are the pressures inside the pores in the unrelaxed state.

The eigenvalues of $\mathbf{G}$ are the inverse relaxation times (i.e., the characteristic frequencies $1/\tau_k = \omega_k$) for the system of pores that relax their pressures in concert. The c_k of (8) weight the individual eigensolutions $\mathbf{\Phi}_k(t)$, so these values serve as a measure of importance for each relaxation mechanism in the system. The total response given by summing over n relaxation mechanisms with characteristic frequencies ω_k and importance a_k is given by

$$M(\omega) = M_r + M_u(1 - \sum_{k=1}^{n}\frac{a_k\omega_k}{\omega_k + i\omega}) \tag{11}$$

$$Q^{-1}(\omega) = \Delta\sum_{k=1}^{n}\frac{a_k\omega_k\omega}{\omega_k^2 + \omega^2}, \tag{12}$$

adapted from *Witte and Richards* [1990], with $a_k = c_k/\sum_{i=1}^{n} c_i$. The modulus defect Δ defined by

$$\frac{\Delta}{2} \equiv \frac{M_u - M_r}{2\sqrt{M_u M_r}}, \tag{13}$$

which is the maximum value of $Q^{-1}(\omega)$ [*Mavko et al.*, 1998]. Equations (11) and (12) serve as our approximations for the total frequency-dependent elastic modulus and attenuation for the system. M_u and M_r are derived from the finite element analyses of *Hammond and Humphreys* [this issue].

3.1. Effect of Scale

Much of what we know about the geometry and connectivity of melt comes from laboratory studies where grain size has been carefully controlled. Typical experimental grain diameters have $d \approx 10^{-5}$ m. Ophiolites studies suggest that natural olivine grain diameters can be roughly 2 orders of magnitude
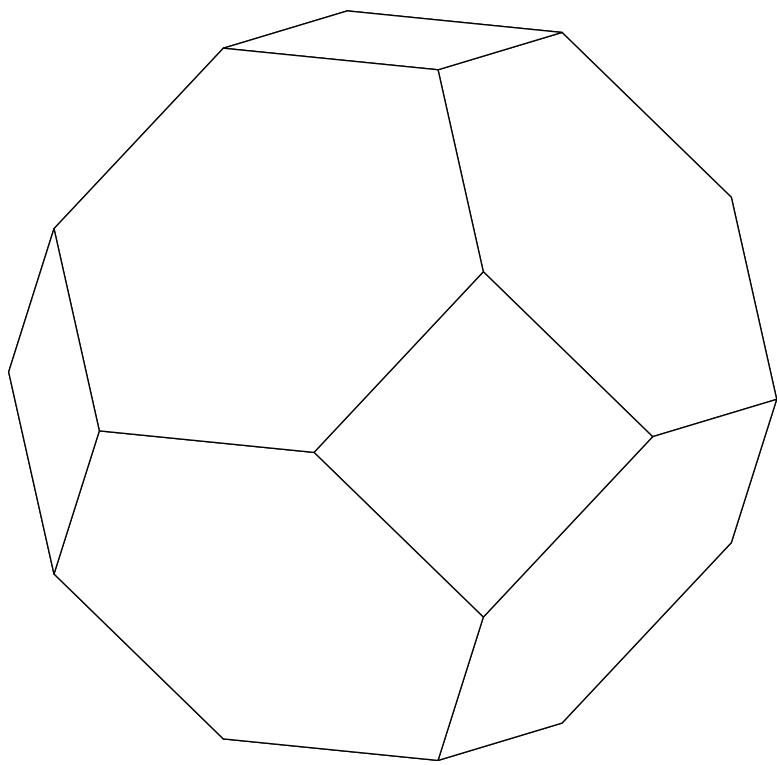
Figure 2: Hammond and Humphreys [2000b]

greater ($d \approx 10^{-3}$ m) [*Nicolas*, 1989]. Thus, while experimentally determined geometries are thought to be similar in shape to those of mantle melts, there may be a great difference in absolute scale between the natural and experimental systems. Fortunately, attenuation due to the melt squirt mechanism is invariant to the absolute scale of melt-matrix system. This is shown with the following example: two differentially pressurized pores each of volume V are joined by a conduit of constant cross-sectional area A and impedance to fluid flow I. We wish to compare the relative effect of changing each component's scale on the characteristic relaxation time of the melt squirt mechanism. For Poiseuille flow through a circular cylindrical conduit the flux of melt through the tube is

$$\Phi = \frac{\pi r^4}{4\eta}\frac{dp}{dx}, \qquad (14)$$

where r is the radius of the tube, dp/dx is the pressure gradient, Φ is the flux of the fluid through the tube, and η is the viscosity of the melt. In this case, the impedance per unit length of conduit is

$$I = 4\eta/\pi r^4. \qquad (15)$$

As the pore cross section becomes noncircular, while preserving the cross-sectional area, the impedance will increase. For the more general tubule we have $I = 4\kappa\eta\pi/A^2$, where $\kappa \geq 1$ is a factor that accounts for the dependence of impedance on the cross-sectional shape of the conduit.

Using (14) and (15), we can evaluate the effect of scale of each of the three key dimensions of the system: the length of the conduit, the diameter of the conduit, and the dimensions of the pores. If we increase the length of the conduit by scale factor h, keeping all other dimensions equal, the pressure gradient is reduced by a factor of $1/h$. Thus fluid flux is reduced by $1/h$, and the relaxation timescale is increased by a factor of h. If, instead, we increase the conduit radius by a factor of h, impedance is reduced by a factor of $1/h^4$, and the relaxation timescale is reduced by $1/h^4$. Finally, if the radii of the pores are increased by h (scaling all three dimensions equally), then their volume increases by h^3. Rescaling the pores, however, has no effect on the amount of strain resulting from far-field stresses so the pressure induced in each pore is unchanged, and the pressure gradient is unaffected. Since the impedance of the conduit is the same and the pressure gradient is the same, the flux of fluid through the conduit does not change, so it takes h^3 times as long to pass the greater

amount of fluid and for pressure to equalize. The total effect of changing the absolute scale of the system is given by the product of these three components. Scaling up all components by h provides scaling of the relaxation time by $hh^31/h^4 = 1$; that is, the timescale of relaxation is unchanged. The competing lengthening and shortening of relaxation times for the melt squirt mechanism cancel, and the melt squirt relaxation time is invariant to absolute scale.

3.2. Results of Attenuation Modeling

We model three cases that represent end-member possibilities for crystal and melt distribution in the upper mantle. The first case is derived from an assumption that the linear dimension of grain size has a Gaussian distribution. The second case assumes that the linear dimension of grain size is log-normally distributed. The third assumes that infrequent large pores are embedded in a network of Gaussian-distributed grain sizes as in the first case. Each is evaluated for its ability to produce the attenuation that is observed in the seismic band.

For each conceptual case a set of self-consistent values is specified for the geometrical and physical parameters of the crystal-melt aggregate with a melt fraction of $\sim 3\%$. These geometric parameters determine $\mathbf{R}$ and $\mathbf{V}$ in (6). The other terms in (6) are determined from the physical properties of the melt η, K_m, connectivity regime $\mathbf{\Gamma}$ (Appendix A), S, and conduit shape scaling factor κ (determined in Appendix B). Absolute scale is not important as noted in section 3.1. Ophiolites studies, however, suggest that olivine grains have diameters of $d \approx 10^{-3}$ m [*Nicolas*, 1989]. We will use this value as an average diameter for the sake of reference. This grain scale with the tetrakaidecahedral connectivity model implies conduit lengths $L = 3.5 \times 10^{-4}$ m. Using melt fraction $F = 0.03$, and a coefficient of partitioning of melt volume between conduits and pores of $\beta = 0.80$, (i.e., most melt in pores) [*Faul et al.*, 1994], we obtain the geometric parameters summarized in Table 1. Initial pore pressures are based on the assumption of randomly oriented biaxial ellipsoids. Because any orientation from 0 to 2π is equally likely, pressures are randomly selected with variance taken from the results of the finite element calculations of *Hammond and Humphreys* [this issue]. In our simulations, 240 pores are connected via 480 conduits. The triple junction tubules are represented with an impedance to flow with $\kappa = 1.75$ (Appendix B).

All parameters needed to determine $\mathbf{G}$ in (6) are

Table 1

now specified, and we can calculate the eigenvalues and thus the relaxation times for the system. The results for the case with Gaussian distribution are shown in Figure 3. Little attenuation occurs in the seismic frequency band. Between 1 and 10 Hz, attenuation increases rapidly, and at $\sim$50 Hz it achieves its peak. This result is inconsistent with nearly constant observed $Q^{-1}(\omega)$, suggesting that attenuation observed with body waves and normal modes is not a result of melt squirt in a Gaussian network.

Another possible case is that the grain size distribution has greater similarity to log-normal distribution than Gaussian. With the same parameters as in the first case (Table 1) except for the distribution of conduit and pore radii, an attenuation band occurs between 10^3 and 10^9 Hz (Figure 3). Since this case has a great many smaller grains, there are a correspondingly greater number of smaller pores and conduits, and thus the importance of shorter relaxation times and higher frequencies is increased. Attenuation in the seismic band is still nearly zero below 1 Hz, where $Q > 1000$, and increases only slightly by 10 Hz.

The presence of a few greatly larger pockets of melt, or localized zones of preferentially aligned inclusions that span many grain diameters, greatly increases relaxation times and provides attenuation closer to the seismic band. In the third case one of the pores from the first case was expanded to 1000 times the average pore size. While the distribution of characteristic frequencies is nearly the same as that of the first case, the response has changed significantly. The attenuation peak has now shifted to $\sim$13 Hz, with significant attenuation in the seismic band. Equalization of pressure requires redistribution of melt to many pores that are connected only indirectly to the large pore, thereby increasing the distance melt must travel. This illustrates that deviations from homogeneous distributions of inclusions cause melt to move over distances larger than the immediate grain scale. This can occur when very large pores exist or when pore orientations collect into spatial domains of preferentially aligned inclusions. These situations provide potential mechanisms by which some relaxation times of the system can be greatly increased.

3.3. Melt Squirt in Bulk Compression

Bulk compression, during P wave propagation, can create variation in the pore pressures when pore aspect ratios vary. We argue below that these pressure differences probably do not drive enough melt squirt

to provide significant relaxation. Thus bulk attenuation due to melt squirt is most likely not important in the seismic band.

Understanding the effect of bulk compression requires knowledge of the distribution of pore aspect ratios, the effect of aspect ratio on internal pore pressure, and the effect of pressure changes on melt squirt relaxation times. The effect of aspect ratio on pore pressure determined from *Eshelby* [1957] shows that there is very little additional change in pore pressure when the aspect ratio goes below 0.1, thus disallowing melt squirt bulk attenuation. If variable aspect ratios occur above 0.1, however, some bulk attenuation might be expected. The relevant results from mantle melting experiments indicate that the proportion of aspect ratios > 0.1 is between 25% and 100% [*Faul*, 1997; *Daines and Kohlstedt*, 1997]. In this case the difference between the relaxed and unrelaxed moduli will increase, increasing the modulus defect (equation (13)). This change alone does not alter relaxation times, however, and thus attenuation remains outside the seismic band. Only if S (equation (A17)) is greatly increased owing to aspect ratio controlled changes in pore pressure will relaxation times be lengthened providing seismic attenuation.

4. Discussion

Our primary result is that for typical conceptions of upper mantle partial melt distribution, relaxation times are too short to provide measurable attenuation in the seismic band. This differs from the conclusion of *O'Connell and Budianski* [1977] that dissipation in a partially molten upper mantle is most probably due to melt flowing between cracks. They, however, used crack aspect ratios distributed evenly from 10^{-4} to 10^{-1}, more extreme than in our modeling. This difference in aspect ratios can account for the difference in our conclusions (Appendix C). In order for melt squirt to cause significant attenuation the relaxation timescales involved in the transport of melt between pores must be lengthened considerably. Appropriate changes in properties that would cause increased transport times include increasing the melt viscosity by orders of magnitude, lengthening transport distances, or increasing conduit impedances. Viscosity of basaltic melts is relatively well constrained by experimental studies and is unlikely to increase by an order of magnitude above our chosen value of 10^2 Pa s. A large degree of interfacial curvature causing conduits to pinch off in the middle would need to be
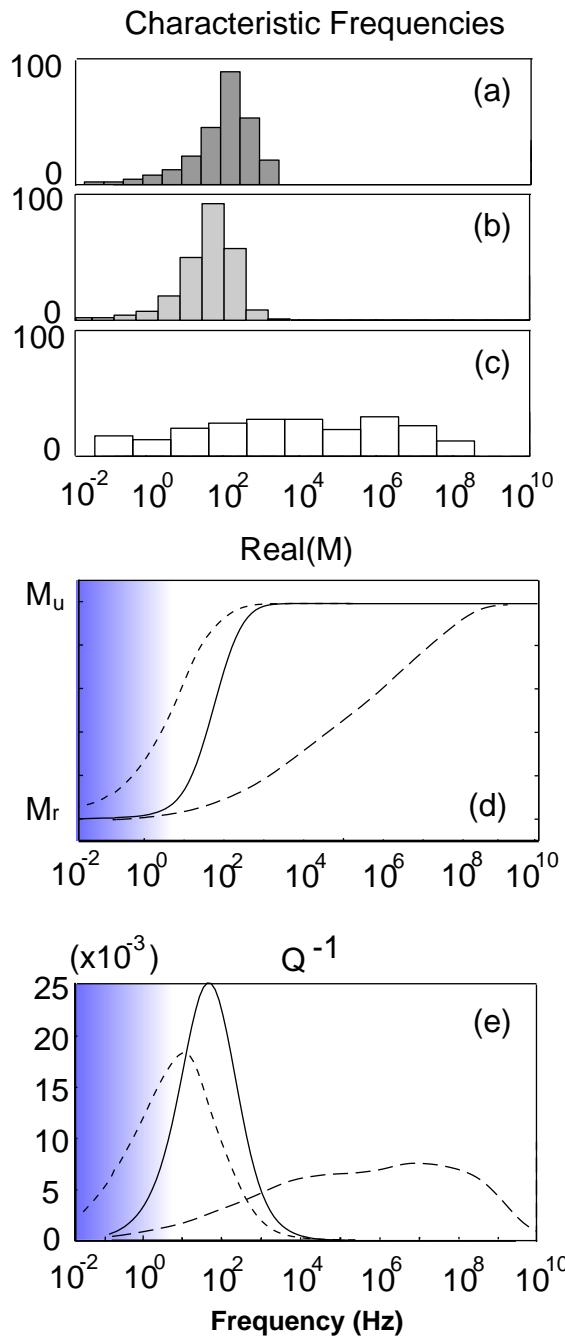
Figure 3: Hammond and Humphreys, [2000b]

a network-wide effect to increase relaxation times; otherwise, melt will find paths of lesser resistance to equalize pore pressure. This might occur if melt topology is modified as a result of long-term changes in melt pore pressure relative to the crystalline matrix [*Waff*, 1980]. One might expect a depth dependence to the set of times, since K_m increases with depth [*Rigden et al.*, 1988]. We have shown, however, in the analysis of parameter sensitivity of Appendix C that K_m does not effect relaxation times. See Appendix C for a more complete discussion of the sensitivity of this modeling to individual parameters.

Segregating the population of inclusions into regions where pores are preferentially aligned can have the effect of increasing transport distance and thus increasing relaxation times. This effect is analogous to the case where a single oversized pore was introduced to the network. Even though the set of relaxation times is nearly identical to the Gaussian case, the relaxation frequency spectrum was changed significantly. For example at 1 Hz, attenuation changed from $Q_S = 361$ for the Gaussian case to $Q_S = 89$ with the single dominant pore. This change in relaxation times is in agreement with the statements made in section 3.1, e.g., adding a single pore 1000 times the volume of the other pores is equivalent to increasing the radius of that pore by a scaling factor of $h = 10$, thus increasing the relaxation times by $h^3 = 1000$. In addition, the mechanisms associated with the passage of melt to pores only indirectly connected to the large pore have increased in importance because it contains a larger proportion of the melt. For example, in Figure 4, melt passing from P_1 to P_4 via P_2 or P_3 has its own characteristic relaxation time. Thus transmitting melt longer distances through the network is possible if pressure gradients provide the incentive. Such a situation can exist if the melt is stratified into horizontal bands [*Waff*, 1980] or if lattice-preferred orientation collects into zones of anisotropic permeability of the order of 10^{-1} to 10^1 m in size. While we can imagine possible ways to increase relaxation times by appealing to regions of aligned melt pockets, it is unlikely that heterogeneous anisotropy on this scale is a common feature in the upper mantle. We conclude that reasonable changes to the distribution of upper mantle partial melt, or in the parameters listed in Table 1, will not provide the lengthing of relaxation times necessary to provide attenuation in the seismic band.

Since there is very little attenuation in the seismic band, and since the peak of attenuation is at frequencies higher than the seismic band, the mod-

ulus excited by observed seismic waves is the relaxed modulus. This translates to the V_P and V_S seismic velocity reductions of 4.3% and 11.4% calculated by *Hammond and Humphreys* [this issue].

This modeling is applicable to low melt fractions between $F = 0\%$ and approximately $F = 3\%$, the range over which the permeability of melt can be represented as tubes connecting low aspect ratio disk-shaped pores. Above this melt fraction the percolation threshold of the disk-shaped pores will be attained [*Faul*, 1997]. At melt fractions greater than the percolation threshold, relaxation times are expected to be much shorter since many new paths for pressure equalization are opened, pushing attenuation even further from the seismic band.

We have assumed here that the distribution of inclusion orientations is random. Experimental studies of partially molten mantle materials indicate that melt in film-like pores become preferentially aligned in the presence of nonhydrostatic stress conditions [*Jin et al.*, 1994; *Kohlstedt and Zimmerman*, 1996; *Bai et al.*, 1997; *Daines and Kohlstedt*, 1997; *Karato et al.*, 1998; *Zimmerman et al.*, 1999]. Preferential alignment does not result, however, in increased melt transport distances or modified inclusion aspect ratios. Furthermore, preferential alignment will tend to enhance connectivity between inclusions and to reduce the variance of induced pore pressure, resulting in decreased relaxation times, smaller modulus defect, and no increase of attenuation in the seismic band.

5. Conclusions

1. Teleseismic waves excite the relaxed modulus of partially molten upper mantle rock. Thus schemes that relate seismic velocity reduction to mantle physical state should employ derivatives of seismic velocity with respect to melt fraction based on relaxed, pressure equilibrated melt, as in the work by *Hammond and Humphreys* [this issue].

2. Since our modeling predicts increasing attenuation with frequency but observed attenuation decreases with frequency, the commonly observed Q in the upper mantle is not due to the melt squirt mechanism.

3. Melt squirt attenuation effects are invariant to the absolute scale of the crystal-fluid assembly. The size of grains does not affect the frequencies that produce melt squirt attenuation. The distribution of grain sizes, however, does affect the relative importance of different relaxation times and thus deter-
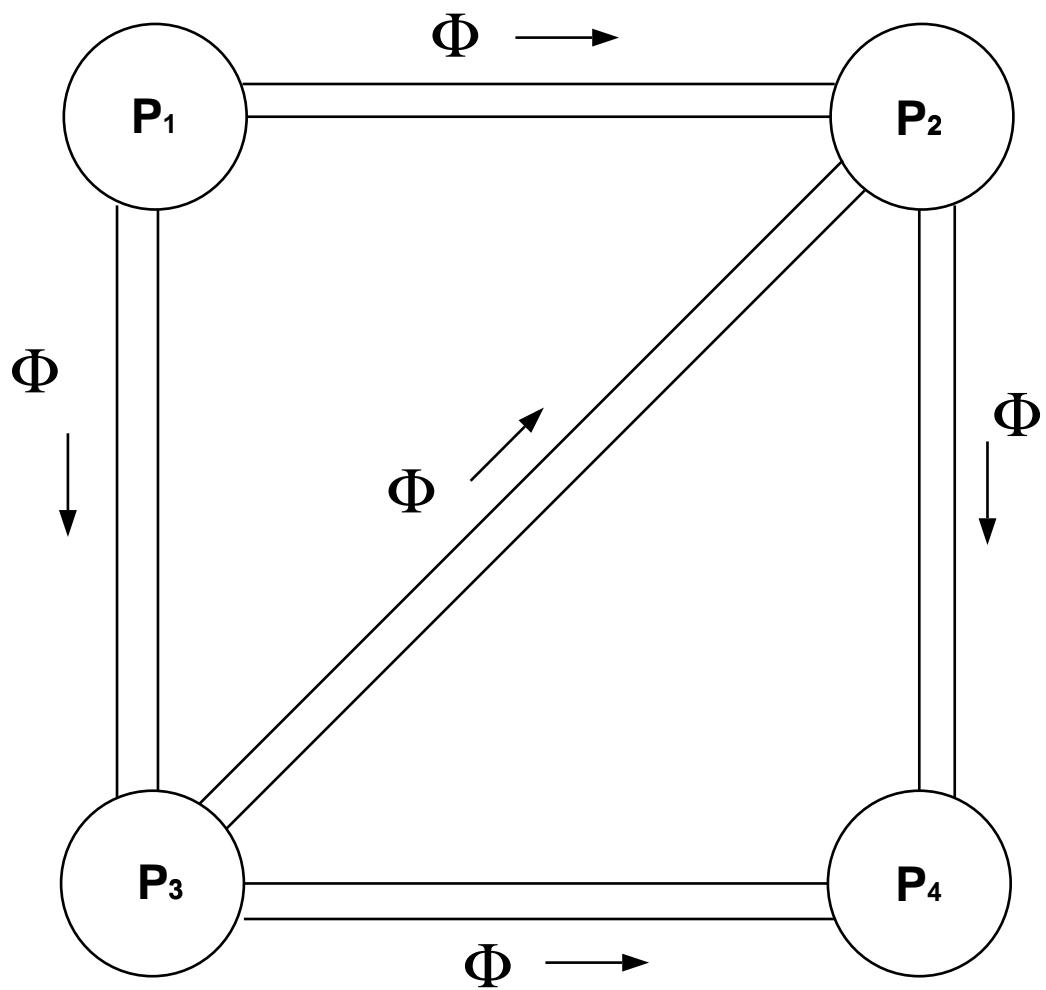
Figure 4: Hammond and Humphreys, [2000b]

mines the dominant frequencies for melt squirt attenuation. The important frequencies are in the band just above the seismic band, assuming that the grain size distribution is Gaussian, and as long as the physical properties of the melt are as listed in Table 1.

4. The frequencies over which melt squirt attenuation are important are strong functions of the aspect ratio of interstitial pores, of the partitioning of melt between narrow conduits and low aspect ratio pores, and of the length scales of fluid transport. Melt squirt is insensitive to the bulk modulus of the melt.

Appendix A: Stress Relaxation of Pores Filled With Melt

A1. Relaxation Time

The physics of fluid relaxation in the pore and conduit network can be described with parameters for the fluid, the conduits, the pores, and the solid matrix. These are the melt viscosity η, melt and solid matrix incompressibility K_m and K_s, fluid flux Φ_j, generalized impedance R_j through the jth conduit, volume V_i, and pressure P_i of the ith pore. For the simplified two-pore system connected via a single conduit the difference in pressure between the pores drives the flux of melt from the first to the second pore:

$$\Phi = \frac{1}{R\eta\kappa}(P_1 - P_2). \tag{A1}$$

The parameter κ corrects for the noncircular cross section of the melt conduit and is determined in Appendix B. The generalized impedance parameter R can be defined by (A1); however, (A1) can also be compared to (14) providing

$$R = \frac{4L}{\pi\kappa r^4}, \tag{A2}$$

where L is the length of the conduit. R is dependent only on the geometry of the tubule and not on any physical properties of the melt or crystal. It is desirable to not assume that conduits have constant cross-sectional shape along their length, and the form of (A1) allows for this. For the purpose of assigning quantities to R, however, in our modeling we do assume constant cross-sectional shape (which can be viewed as the effective cross-sectional shape for conduits that do change along their length). By using $\kappa = 1.75$ in (A2) we are assuming that the conduit has the triple junction cross section (Appendix B) and constant cross-sectional shape.

Rearranging (A1) and differentiating with respect to time provides

$$\frac{d\Phi}{dt} = \frac{1}{\eta\kappa R}\left(\frac{dP_1}{dt} - \frac{dP_2}{dt}\right). \tag{A3}$$

The derivative of pressure with respect to time is related to the flux through the tube with

$$\frac{dP}{dt} = \Phi\frac{dP}{dV}. \tag{A4}$$

We model the transition from the unrelaxed to the relaxed state, so the derivative on the right side of (A4) becomes

$$\frac{dP}{dV} = \frac{P_r - P_u}{V_r - V_u}, \tag{A5}$$

where the subscripts r and u refer to the relaxed and unrelaxed states. We also presume that all melt pockets are connected, so $P_r = 0$ (we have removed the background hydrostatic pressure field), and

$$\frac{dP}{dV} = \frac{P_u}{V_u - V_r}. \tag{A6}$$

Substituting (A6) into (A4) and into (A3) gives our first-order linear differential equation

$$\frac{d\Phi}{dt} = -\omega\Phi, \tag{A7}$$

where

$$\omega = \frac{1}{\eta\kappa R}\left[\frac{P_{1u}}{V_{1u} - V_{1r}} + \frac{P_{2u}}{V_{2u} - V_{2r}}\right] \tag{A8}$$

is the inverse of the relaxation time constant (characteristic frequency) for the system since the solution to (A7) is $\Phi(0)e^{-\omega t}$.

The pore pressure and volume terms in (A8) can be recast as equivalent hydrostatic strains of the melt associated with transition from the unrelaxed to the relaxed state

$$P_u = -K_m\varepsilon_u, \tag{A9}$$

$$\varepsilon_u = \frac{V_u - V_0}{V_0}, \tag{A10}$$

$$\varepsilon_r = \frac{V_r - V_0}{V_0}, \tag{A11}$$

where V_0 is the original undeformed pore volume and V_r and V_u are the volumes in the relaxed and unrelaxed states. Note that expansive strains are positive so a contracting volume provides positive pressure. So now

$$\omega = \frac{K_m}{\eta\kappa R}\left[\frac{\varepsilon_{1u}}{V_{10}(\varepsilon_{1r} - \varepsilon_{1u})} + \frac{\varepsilon_{2u}}{V_{20}(\varepsilon_{2r} - \varepsilon_{2u})}\right], \tag{A12}$$

where ε_{iu} is the volumetric strain of the liquid inside pore i in the unrelaxed state.

To simplify, we use pores shaped like biaxial ellipsoids of aspect ratio $\alpha = 0.1$ (with axes $a = b > c$) embedded in an elastic medium with the c axis in the x-z plane. Pure shear is induced by contraction along the z axis and extension along the x axis (Figure A1). We can approximate the volumetric strain inside the pores as functions of orientation θ_i with respect to the pure shear

$$\varepsilon_{iu} = E_u \cos(2\theta_i) \qquad (A13)$$
$$\varepsilon_{ir} = E_r \cos(2\theta_i), \qquad (A14)$$

where $\theta_i = 0$ when the minor axis of the ellipsoid is aligned with the axis of maximum contraction. Thus E_u and E_r are defined via (A13) and (A14) as the maxima of the volumetric strains inside the pores in the unrelaxed and relaxed states, respectively. Substituting (A13) and (A14) into (A12) provides

$$\omega = \frac{K_m}{\eta \kappa R}\left[\frac{E_{1u}}{V_{10}(E_{1r} - E_{1u})} + \frac{E_{2u}}{V_{20}(E_{2r} - E_{2u})}\right]. (A15)$$

The orientations of the ellipses have dropped out since it is the ratio of the difference in strain between the unrelaxed and relaxed states controls the relaxation time. Thus the relaxation time is not dependent on pore orientation. Pore orientation does, however, effect initial pore pressure, i.e., the $\Phi(0)$ term in (10), and in that way controls the importance of the relaxation of that specific pore to the whole system.

Since all pores have the same aspect ratio in our model, they have identical maximum strains within them so all $E_{iu}/(E_{ir} - E_{iu})$ are the same and

$$\omega = \frac{K_m}{S \eta \kappa R}\left[\frac{1}{V_1} + \frac{1}{V_2}\right] \qquad (A16)$$

$$S = \frac{(E_r - E_u)}{E_u}, \qquad (A17)$$

where S is the parameter that represents the percentage change in strain inside the inclusion between the relaxed and the unrelaxed states. In this way we have contained all the properties of the solid and liquid elastic interaction that are relevant to the melt squirt relaxation times into one parameter S.

A2. Representing the Connectivity of Many Pores

When more than two pores are present, then the pressure and melt content of each pore can be effected by flow into or out of several conduits. A simplified example of four pores connected by five conduits is shown in Figure 4. Each conduit has a positive prescribed direction as shown with arrows in Figure 4.

The flux through each conduit is represented according to (A1) by

$$\begin{aligned}
\Phi_1 &= \tfrac{1}{\eta \kappa R_1}(P_1 - P_2) \\
\Phi_2 &= \tfrac{1}{\eta \kappa R_2}(P_2 - P_4) \\
\Phi_3 &= \tfrac{1}{\eta \kappa R_3}(P_1 - P_3) \qquad (A18) \\
\Phi_4 &= \tfrac{1}{\eta \kappa R_4}(P_3 - P_4) \\
\Phi_5 &= \tfrac{1}{\eta \kappa R_5}(P_3 - P_2).
\end{aligned}$$

The fluxes change pressure in pores by removing or adding melt. Thus for each pore we use (A4) and (A6). Equating (A8) with (A16) and matching terms yields

$$\frac{P_{iu}}{V_{iu} - V_{ir}} = \frac{K_m}{SV_i}. \qquad (A19)$$

This gives the rate of change of pressure in each pore as

$$\begin{aligned}
\frac{dP_1}{dt} &= \frac{K_m}{SV_1}[-\Phi_1 - \Phi_3] \\
\frac{dP_2}{dt} &= \frac{K_m}{SV_2}[\Phi_1 - \Phi_2 + \Phi_5] \\
\frac{dP_3}{dt} &= \frac{K_m}{SV_3}[\Phi_3 - \Phi_4 + \Phi_5] \qquad (A20) \\
\frac{dP_4}{dt} &= \frac{K_m}{SV_4}[\Phi_2 + \Phi_4].
\end{aligned}$$

Differentiating (A18) and substituting in (A20) yields a set of equations that can be represented as

$$\frac{d\mathbf{\Phi}}{dt} = \mathbf{G}\mathbf{\Phi} \qquad (A21)$$

where

$$\mathbf{G} = -\frac{K_m}{\eta \kappa S}\mathbf{R}^{-1}\mathbf{\Gamma}\mathbf{V}^{-1}\mathbf{\Gamma}^{\mathbf{t}}, \qquad (A22)$$

where generalized impedances for each conduit are stored in a diagonal matrix $\mathbf{R}$ and the pore volumes are stored along the diagonal of matrix $\mathbf{V}$. The connectivity of the pores is contained in $\mathbf{\Gamma}$, explained below in more detail. This system of linear differential equations solves the time-dependent flow problem for the vector containing the melt fluxes in the conduits $\mathbf{\Phi}$.

When there are a great many pores present and they are connected according to the tetrakaidecahedral coordination, each pore is connected to four conduits, and each conduit is connected to two pores. Thus if n is the total number of pores, then there are $2n$ conduits. We can represent the connectivity of all pores to one another with the matrix $\mathbf{\Gamma}$. If pore i and
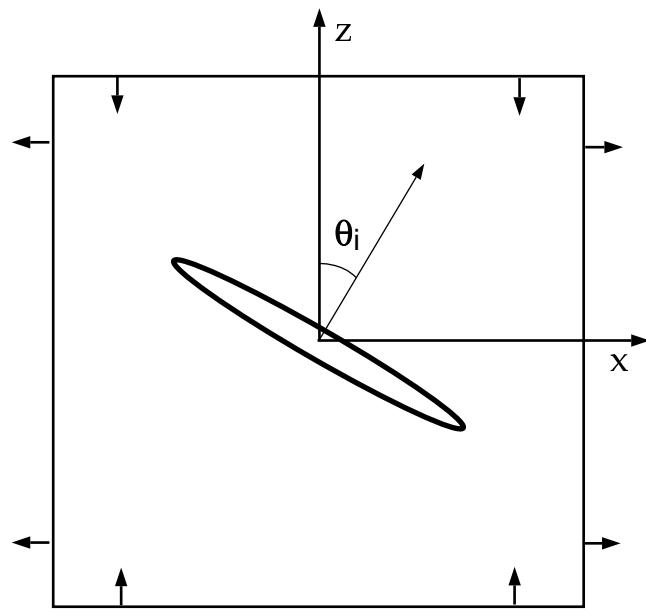
Figure A1: Hammond and Humphreys, [2000b]

pore j are connected via a conduit, then $\Gamma_{ij} = \pm 1$, with the sign dependent on the prescribed positive direction for melt flowing through the tube. Γ is a $2n$ by n matrix, with the rows of Γ each representing a single conduit and thus having only two nonzero entries, one positive and one negative. The columns of Γ represent individual pores, so that the number of nonzero entries in a column represents the number of conduits connecting at this pore. In this case, with tetrakaidecahedral coordination, there will always be four nonzero entries, whose signs represent the oriented direction for positive flux in or out of this pore. Γ can be randomly generated by beginning with any matrix that satisfies this criterion and then permuting the rows and columns, since these transformations do not alter the connectivity regime (i.e., the same number of conduits will connect at each pore).

Appendix B: Impedance of a Cuspate Tubule

The increase in fluid dynamic impedance due to the cuspateness of tubule cross section is calculated with visco-elastic finite elements. Three-dimensional tubes of both circular and triangular cuspate cross section are constructed. The shape of the triangular cuspate tube with unit radius is defined as

$$x = \cos(\theta) + \frac{1}{2+\epsilon}\cos(2\theta) \qquad (B1)$$

$$y = -\sin(\theta) + \frac{1}{2+\epsilon}\sin(2\theta) \qquad (B2)$$

Mavko, [1980]. The shape approaches a circle when $\epsilon \to \infty$ and is most cuspate when $\epsilon = 0$. Figure B1 illustrates these shapes.

To examine the difference in flow properties between the cuspate and circular tubules, a pressure gradient is applied along the fluid inside tubes of both shapes, with the same cross sectional area. The finite element calculation provides the velocities for every point inside the tube, from which the volumetric flux of fluid down the tube is calculated. The ratio of flux through the circular tube to the flux through the cuspate tubes is $\kappa = 1.75$. Down tube velocity for each cross section is shown in Figure B1. These calculations were performed with the three-dimensional viscoelastic finite element program GAEA/BORG developed by *Saucier* [1991] and *Palmer* [1997].

Appendix C: Sensitivity Analysis

To investigate the inherent sensitivity of the characteristic frequencies to each parameter, we examine

$$\frac{X}{\omega}\frac{d\omega}{dX}, \qquad (C1)$$

where X is the parameter in question. The results are listed in Table 1.

In most cases the determination of the sensitivity is straightforward using (A16). In some cases, however, the parameter analyzed affects more than one variable in (A16), making calculation of the sensitivity slightly more complicated. For example, to determine the dependence of characteristic frequency on melt fraction, we notice that ω is a function of the pore volume v_p and conduit volume v_c and that these are, in turn, dependent on F. The sensitivity is given by

$$\frac{F}{\omega}\frac{d\omega}{dF} = \frac{F}{\omega}\left[\frac{\partial\omega}{\partial v_p}\frac{dv_p}{dF} + \frac{\partial\omega}{\partial v_c}\frac{dv_c}{dF}\right]. \qquad (C2)$$

Partial derivatives with respect to F are easily derived from the definition of $F \equiv (v_p + v_c)/v_0$, where v_0 is the total solid plus melt volume and the definition of $\beta \equiv v_p/(v_p + v_c)$. The two partial derivatives of ω are given in Table 1 for the parameters v_p and v_c. The answer simplifies to

$$\frac{F}{\omega}\frac{d\omega}{dF} = 1. \qquad (C3)$$

Sensitivity of ω to pore aspect ratio α is determined in the range of aspect ratios $1 < \alpha < 10^{-3}$. Characteristic frequency is a function of S and σ_p, which are both, in turn, dependent on α. Working with $\log(\alpha)$ provides

$$\frac{\log(\alpha)}{\omega}\frac{d\omega}{d\log(\alpha)} = \frac{\log(\alpha)}{\omega}\left[\frac{\partial\omega}{\partial S}\frac{dS}{d\log(\alpha)} + \frac{\partial\omega}{\partial \sigma_p}\frac{d\sigma_p}{d\log(\alpha)}\right]. \qquad (C4)$$

The right-hand term goes to zero, since sensitivity to σ_p vanishes (Table 1), and sensitivity to S is known from Table 1, so

$$\frac{\log(\alpha)}{\omega}\frac{d\omega}{d\log(\alpha)} = -\frac{\log(\alpha)}{S}\frac{dS}{d\log(\alpha)} \qquad (C5)$$

Sensitivity of S to $\log(\alpha)$ is determined numerically with the equations of *Eshelby* [1957] and *Wu* [1966], providing

$$\frac{\log(\alpha)}{\omega}\frac{d\omega}{d\log(\alpha)} = -5\log(\alpha), \qquad (C6)$$
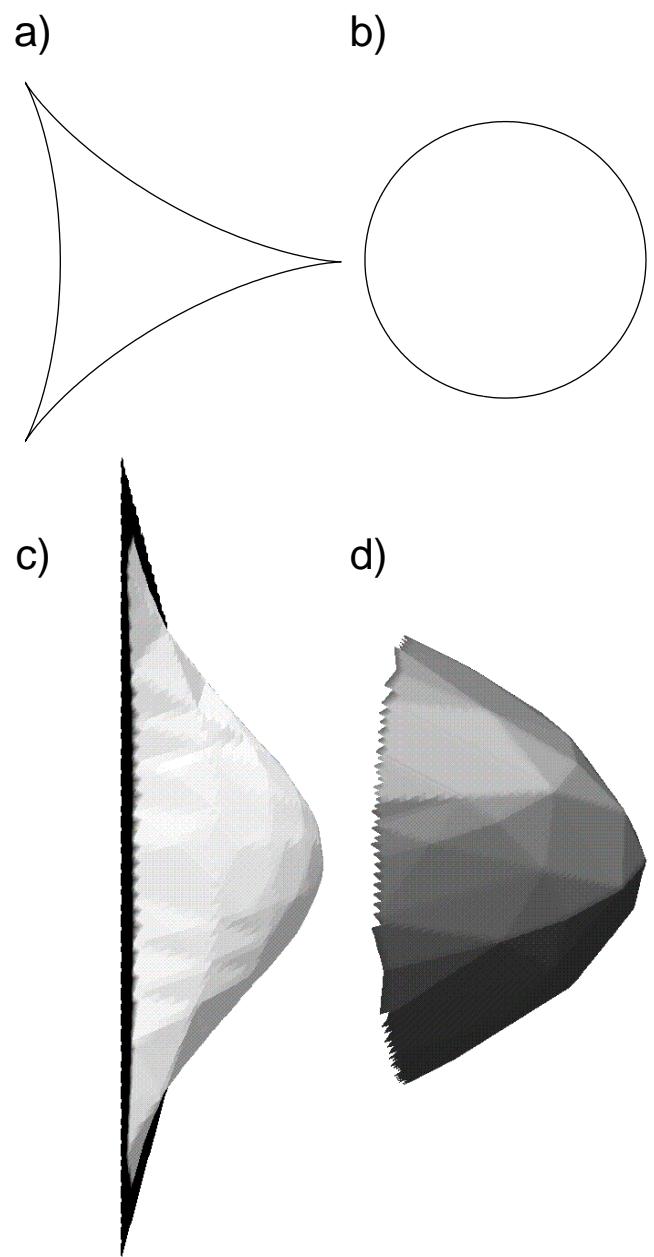
a)

b)

c)

d)

Figure B1: Hammond and Humphreys, [2000b]

which, for $\alpha = 0.10$, yields the value in Table 1. Relaxation frequencies become less sensitive to α as the pores become more spherical.

The partition coefficient β has the greatest effect of all parameters on the characteristic frequencies of melt squirt attenuation. Its derivation is similar to that for the effect of melt fraction, except that in this case the parameters β do not cancel. Sensitivity to β is given by

$$\frac{\beta}{\omega}\frac{d\omega}{d\beta} = \frac{\beta + 1}{\beta - 1}. \tag{C7}$$

This has an increasingly negative value as $\beta \to 1$. As β increases, the radii of the pores increase, while the radii of the conduits decrease, both contributing to increased relaxation times. When the radius of the conduits approaches zero the conduit impedance increases very rapidly. For this reason, when $\beta = 0.80$, the sensitivity of characteristic frequency to β is -9. Thus characteristic frequencies are more sensitive to changes in the partitioning of the melt volume between pores and conduits β than to any other model parameters.

Sensitivity values for the standard deviations of the pore and conduit radii, σ_p and σ_c, are not shown since changes in the distribution of radii affect many characteristic frequencies rather than a single frequency. Therefore the whole distribution of characteristic frequencies must be calculated, as was discussed in section 3.3.

C1. Effect of Melt Bulk Modulus

The melt bulk modulus K_m has no effect on the characteristic frequencies of melt squirt attenuation. Applying our sensitivity analysis strategy, from (A16) we see that K_m is in the numerator, and thus we might expect sensitivity of $+1$ as a result. K_m also effects S, however, so the sensitivity is given by

$$\frac{K_m}{\omega}\frac{d\omega}{dK_m} = \frac{K_m}{\omega}\left[\frac{\partial\omega}{\partial K_m} + \frac{\partial\omega}{\partial S}\frac{dS}{dK_m}\right] = 1 - \frac{K_m}{S}\frac{dS}{dK_m}. \tag{C8}$$

We find the right-hand term by numerically calculating S as a function of K_m and then differentiating. S, as defined by (A17), is the percentage change in volumetric strain of the fluid during transition from the unrelaxed to the relaxed state. We therefore obtain S by calculating the maximum strains for the fluid inside the pore in the unrelaxed E_u and relaxed E_r states. This is accomplished by applying the relationships of *Eshelby* [1957] and *Wu* [1966], for the

response of an ellipsoidal inclusion embedded in an infinite elastic medium. Maximum hydrostatic strains inside the pore occur when we induce pure shear by providing shortening of the solid along the short axis of the oblate ellipsoid ($\varepsilon_{zz} = -0.1$) and lengthening along one of the other axes ($\varepsilon_{xx} = 0.1$). We use a biaxial ellipsoid with aspect ratio $\alpha = 0.1$, containing material with Poisson's ratio $\nu = 0.5$ (a fluid). We find the interior strain for fluids with K_m/K_s varying from 10^{-6} to 10^1. Results are presented in Figure C1.

Note that for these conditions the hydrostatic strains inside the pore are positive, indicating that when far-field strain in the solid is contractional along the short axis, net expansive strain inside the pore results. This is due to the competing effect of the solid contracting in the direction perpendicular to the lengthening direction and thereby pulling away from the pore center.

The values needed to calculate S as a function of K_m are in Figure C1a. E_r is independent of K_m since it is the maximum strain of the fluid associated with the relaxed state. This occurs when pressure is equalized between the inclusions so it is always the value of strain in the limit that $K_m \to 0$. E_u is the unrelaxed maximum strain and is always a function of K_m. The resulting values for S are shown in Figure C1b. As it turns out, S is proportional to K_m, and thus the rightmost term of (C8) equals one, leaving

$$\frac{K_m}{\omega}\frac{d\omega}{dK_m} = 0. \tag{C9}$$

This result makes intuitive sense when we imagine the competing effects of changing K_m. For example, increasing K_m provides greater pressure in the pores resulting from a given applied strain, tending to reduce relaxation times. S also increases with K_m, however, so the magnitude of the difference between the unrelaxed and relaxed states increases as K_m increases, thereby increasing the relaxation time. These effects cancel one another, providing zero sensitivity to the melt bulk modulus.

(a)

Hydrostatic Strain

ε_{zz}

ε_{xx}

(b)

S

Km/Ks
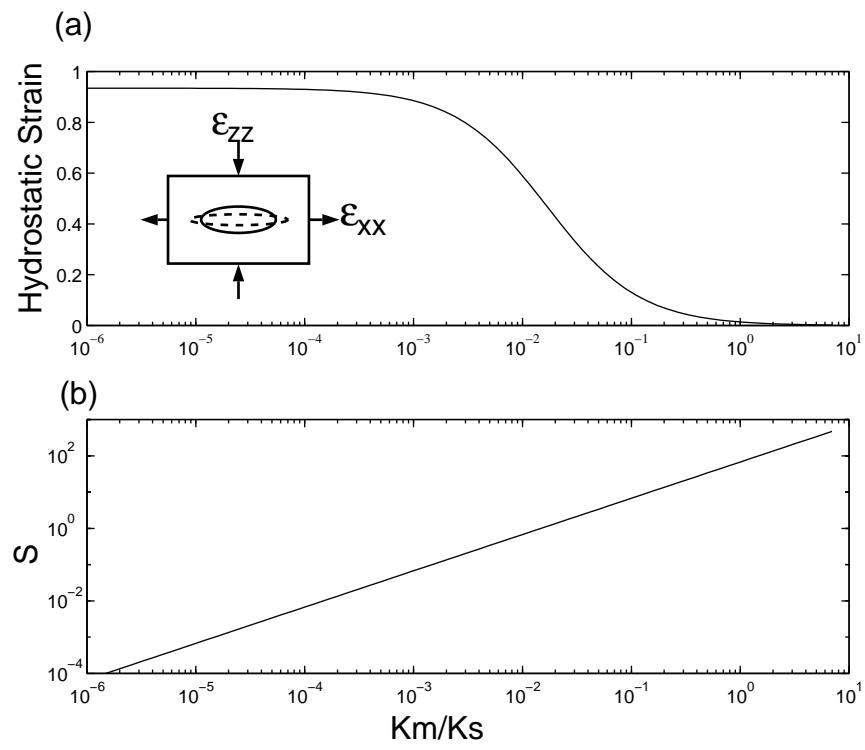
References

Aki, K., and P.G. Richards, *Quantitative Seismology, Theory and Methods*, vol. 1, 557 pp., W.H. Freeman, New York, 1980.

Anderson, D.L., and J.W. Given, Absorption band Q model for the Earth, *J. Geophys. Res.*, *87*, 3893-3904, 1982.

Anderson, D.L., and R.S. Hart, Q of the Earth, *J. Geophys. Res.*, *83*, 5869-5882, 1978.

Bai, Q., Z.-M. Jin, and H.W. Green II, Experimental investigation of the rheology of partially molten peridotite at upper mantle pressures and temperatures, in *Deformation-Enhanced Fluid Transport in the Earth's Crust and Mantle, Mineral. Soc. Ser.*, 8, edited by M.B.Holness, pp. 40-61, Chapman and Hall, New York, 1997.

Cara, M., Lateral variations of S velocity in upper mantle from higher Rayleigh modes, *Geophys. J. R. Astron. Soc.*, *57*, 649-670, 1979.

Daines, M.J., and D.L. Kohlstedt, Influence of deformation on melt topology in peridotites, *J. Geophys. Res.*, *102*, 10,257-10,271, 1997.

Eshelby, J.D., The determination of the elastic field of an ellipsoidal inclusion and related problems, *Proc. R. Soc. London, Ser. A*, *241*, 376-396, 1957.

Faul, U.H., Permeability of partially molten upper mantle from experiments and percolation theory, *J. Geophys. Res.*, *102*, 10,299-10,311, 1997.

Faul, U.H., D.R. Toomey, and H.S. Waff, Intergranular basaltic melt is distributed in thin, elongated inclusions, *Geophys. Res. Lett.*, *21*, 29-32, 1994.

Frank, F.C., Two-component flow model for convection in the Earth's upper mantle, *Nature*, *220*, 350-352, 1968.

Hammond, W.C., and E.D. Humphreys, Upper mantle seismic wave velocity: Effect of realistic partial melt geometries, *J. Geophys. Res.*, this issue.

Hirth, G., and D.L. Kohlstedt, Experimental constraints on the dynamics of the partially molten upper mantle: Deformation in the diffusion creep regime, *J. Geophys. Res.*, *100*, 1981-2001, 1995a.

Hirth, G., and D.L. Kohlstedt, Experimental constraints on the dynamics of the partially molten upper mantle, 2, Deformation in the dislocation creep regime, *J. Geophys. Res.*, *100*, 15,441-15,449, 1995b.

Jackson, D.D., and D.L. Anderson, Physical mechanisms of seismic wave attenuation, *Rev. Geophys.*, *8*, 1-63, 1970.

Jin, Z.-M., H.W. Green II, and Y. Zhou, Melt topology in partially molten mantle peridotite during ductile deformation, *Nature*, *372*, 164-167, 1994.

Kanamori, H., and D.L. Anderson, Importance of physical dispersion in surface wave and free oscillation problems: review, *Rev. Geophys.*, *15*, 105-112, 1977.

Karato, S., and H.A. Spetzler, Defect microdynamics in minerals and solid-state mechanisms of seismic wave attenuation and velocity dispersion in the mantle, *Rev.*

Geophys., *28*, 399-421, 1990.

Karato, S., S. Zhang, M.E. Zimmerman, M.J. Daines, and D.L. Kohlstedt, Shear deformation of mantle materials: Towards structural geology of the mantle, *Pure Appl. Geophys.*, *14*, 589-603, 1998.

Kohlstedt, D.L., Structure, rheology, and permeability of partially molten rocks at low melt fractions, in *Mantle Flow and Melt Generation at Mid-Ocean Ridges, Geophys. Monogr. Ser.*, vol. 71, edited by J. Phipps Morgan, D.K. Blackman, and J.M. Sinton, pp. 1-65, AGU, Washington, DC., 1992.

Kohlstedt, D.L., and M.E. Zimmerman, Rheology of partially molten mantle rocks, *Annu. Rev. Earth Planet. Sci.*, *24*, 41-62, 1996.

Mavko, G.M., Velocity and attenuation in partially molten rocks, *J. Geophys. Res.*, *85*, 5173-5189, 1980.

Mavko, G.M., and A. Nur, Melt squirt in the asthenosphere, *J. Geophys. Res.*, *80*, 1444-1448, 1975.

Mavko, G.M., T. Mukerji, and J. Dvorkin, *The Rock Physics Handbook: Tools for Seismic Analysis in Porous Media*, 329 pp., Cambridge Univ. Press, New York, 1998.

Nicolas, A., *Structures of Ophiolites and Dynamics of Oceanic Lithosphere*, 367 pp., Kluwer Acad., Norwell, Mass., 1989.

Nishimura, C.E., and D.W. Forsyth, The anisotropic structure of the upper mantle in the Pacific, *Geophys. J. Int.*, *96*, 203-229, 1989.

O'Connell, R.J., and B. Budianski, Viscoelastic properties of fluid-saturated cracked solids, *J. Geophys. Res.*, *82*, 5719-5735, 1977.

Palmer, R.L., Studies of the kinematics and dynamics of southern California and northern Baja, Mexico, Ph.D. thesis, 147 pp., Univ. of Oreg., Eugene, June 1997.

Rigden, S.M., J. Thomas, and E.M. Stopler, Shock compression of molten silicate: Results for a model basaltic composition, *J. Geophys. Res.*, *93*, 367-382, 1988.

Saucier, F.J., Studies of plate dynamics at continental margins, Ph.D. thesis, 276 pp., Univ. of Oreg., Eugene, Aug. 1991.

Schmeling, H., Numerical models on the influence of partial melt on elastic, anelastic and electrical properties of rocks, part I, Elasticity and anelasticity, *Phys. Earth Planet. Inter.*, *41*, 34-57, 1985.

Sobolev, S.V., H. Zeyen, G. Stoll, F. Werling, R. Althern, and K. Fuchs, Upper mantle temperatures from teleseismic tomography of French Massif Central including effects of composition, mineral reactions, anharmonicity, anelasticity and partial melt. *Earth Planet. Sci. Lett.*, *139*, 147-163, 1996.

Solomon, S.C., and M.N. Toksöz, Lateral variation of attenuation of P and S waves beneath the United States, *Bull. Seismol. Soc. Am.*, *60*, 819-838, 1970.

Waff, H.S., Effects of gravitational field on liquid distribution in partial melts within the upper mantle, *J. Geophys. Res.*, *85*, 1815-1825, 1980.

Waff, H.S., and J.R. Bulau, Equilibrium fluid distribution in ultramafic partial melt under hydrostatic stress conditions, *J. Geophys. Res.*, *84*, 6109-6114, 1979.

Webb, S.C., and D.W. Forsyth, Structure of the upper mantle under the EPR from waveform inversion of regional events, *Science*, *280*, 1227-1229, 1998.

Witte, D.C., and P.G. Richards, The pseudospectral method for simulating wave propagation, *Comput. Acoust.*, *3*, 1-18, 1990.

Wu, T.T., The effect of inclusion shape on the elastic moduli of a two-phase material, *Int. J. Solids Struct.*, *2*, 1-8, 1966.

Zimmerman, M.E., S. Zhang, D.L. Kohlstedt, and S. Karato, Melt distribution in mantle rocks deformed in shear, *Geophys. Res. Lett.*, *26*, 1505-1508, 1999.

W.C. Hammond and E.D. Humphreys, Department of
Geological Sciences, University of Oregon, Eugene OR 97405. (bill@newberry.uoregon.edu)

Figure 1. Viscoelastic model for partially molten upper mantle rock. (a) An applied step in strain ε results in (b) a step in stress σ followed by an exponential decay over time t. Stages of mechanical response: (c) undeformed, (d) glued, with shear stress still present in the fluid, (e) unrelaxed with shear stress within the pore gone, (f) relaxed with pressure equalized between pores. The vertical light grey line highlights the shear deformation inside and around one pore at each step.

Figure 2. Tetrakaidecahedral model for space-filling olivine crystal. Also known as a truncated octohedron, the shape has 14 faces and 36 edges.

Figure 3. Results of modeling of melt squirt anelasticity. Histograms of characteristic frequencies for the (a) Gaussian, (b) single large pore added, and (c) lognormal cases. (d) Real part of elastic modulus, and (e) attenuation function $Q^{-1}(\omega)$, with Gaussian case (solid line), single large pore embedded (short dashed line), and lognormal distribution of grain sizes (long dashed line). Seismic band up to 10 Hz is shaded for clarity.

Figure 4. Ellipsoidal pore space in an elastic solid medium. Pure shear induced via contraction along z axis, extension along x axis. Short axis of pore i is oriented at angle θ_i with respect to applied shear.

Figure A1. Example with four pores and five conduits connected in a network. Arrows indicate positive melt flux Φ_i direction through conduit i. Pore are represented by P_j.

Figure B1. Cross-sectional shapes for the (a) cuspate ($\epsilon = 0$) and the (b) circular ($\epsilon \to \infty$) tubes. (c) and (d) Velocity of the fluid throughout the tube. For tubes with the same cross-sectional area and pressure gradient, $\sim 75\%$ more melt flows through the circular tube in the same amount of time.

Figure C1. (a) Volumetric strain inside a biaxial ellipsoid with aspect ratio $\alpha = 0.10$ as a function of melt bulk modulus K_m/K_s. Inset shows results assuming that far-field strain is $\epsilon_x, \epsilon_y, \epsilon_z = [0.1, 0, -0.1]$. (b) S parameter as a function of melt bulk modulus.

Table 1. Parameters Used in Modeling Melt Squirt Anelasticity

Description	Parameter Value	Sensitivity ($\frac{X}{\omega}\frac{d\omega}{dX}$)
Grain size	$d = 0.001$ m	0
Conduit length	$L = 3.53 \times 10^{-4}$ m	-1
Melt fraction	$F = .03$	+1
Fluid viscosity	$\eta = 100$ Pa s	-1
Melt bulk modulus	$K_m = 40$ GPa	0
Biaxial pore aspect ratio	$\alpha = 0.10$	+5
Pore/conduit partition coefficient	$\beta = 0.80$	-9
Mean pore radius	$\bar{r}_p = 1.420 \times 10^{-4}$ m	-3
Mean pore volume	$\bar{v}_p = 1.200 \times 10^{-9}$ m^3	-1
Pore radius s.d.	$\sigma_{rp} = 3.550 \times 10^{-5}$ m	$\cdots$
Mean conduit radius	$\bar{r}_c = 1.500 \times 10^{-5}$ m	+4
Mean conduit volume	$\bar{v}_c = 3.000 \times 10^{-10}$ m^3	+2
Conduit radius stand. dev.	$\sigma_{rc} = 3.750 \times 10^{-6}$ m	$\cdots$
Mean conduit impedance	$\bar{R} = 3.97 \times 10^{16}$ m^{-3}	-1
Mean initial pore pressure	$\bar{p} = 0$	0
Initial pore pressure s.d.	$\sigma_p = 2.5$ GPa	0
Conduit noncircular impedance	$\kappa = 1.75$	-1
Differential hydrostatic strain	$S = 23.1$	-1

The parameters $L, \bar{v}_p, \bar{v}_c, R$, and S are calculated from the other input parameters. Sensitivity is defined in (16).